ACS APPLIED MATERIALS & INTERFACES

www.acsami.org Research Article

# Optoelectronic Properties of Atomic Layer Deposited and Sputtered $MoS_2$ Films

Crystal Alicia Nattoo,[#] Tara Peña,[#] Koosha Nassiri Nazif, Xiangjin Wu, Sepideh Rahimisheikh, Giulio D'Acunto, Stacey F. Bent, Joke Hadermann, and Eric Pop*

Cite This: *ACS Appl. Mater. Interfaces* 2025, 17, 47347−47354 Read Online

ACCESS | Metrics & More | Article Recommendations | Supporting Information

**ABSTRACT:** Large-area growth techniques are needed to bring transition metal dichalcogenide (TMD) films into future applications, but some of these methods have not been sufficiently studied. Here, we evaluate and compare few-layer $MoS_2$ films (<3 nm thick) grown by atomic layer deposition (ALD) and radio frequency (RF) sputtering, using optical, topographical, X-ray spectroscopy, transmission electron microscopy, and electrical device characterization. The electron mobility of ALD films improves 3-fold with rapid thermal annealing, and these improvements are correlated with changes in their Raman spectra, such as a decrease in both the shoulder-to-$E_{2g}$ and LA(M)-to-$A_{1g}$ intensity ratios. On the other hand, the sputtered films had lower mobility and lower transistor current on/off ratio than the ALD samples, and the thermal annealing worsened both their surface roughness and electrical behavior. This work illustrates the utility of nondestructive materials characterization (e.g., Raman, with complementary techniques) to obtain a better picture of material quality before performing time-consuming device fabrication and electrical testing on emerging TMD films.

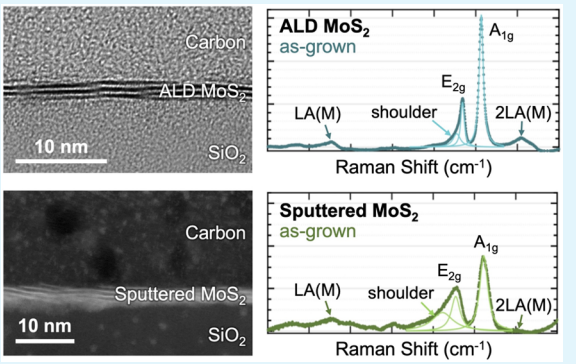


**KEYWORDS:** *defect metrology, transition metal dichalcogenides, atomic layer deposition, RF sputtering, Raman spectroscopy, electrical characterization*



## INTRODUCTION

Layered, atomically thin two-dimensional (2D) semiconductors have emerged in recent years with the promise of better charge mobility than conventional semiconductors at few-nanometer or subnanometer thickness.[1] These materials can also be synthesized at sufficiently low temperatures as to be compatible with back-end-of-line (BEOL) or three-dimensional (3D) heterogeneous monolithic integration in conventional electronics,[2,3] or even with more temperature-sensitive flexible substrates.[4−9] Nevertheless, much research on 2D semiconductors, such as transition metal dichalcogenides (TMDs), has relied on techniques such as mechanical exfoliation, which are not scalable to uniform, large-area films.

While chemical vapor deposition (CVD) has produced films for lab-scale experimentation,[10−14] the growth temperature often exceeds 500 °C, which is incompatible with heterogeneous 3D and flexible substrate integration. Instead, techniques such as metal-organic CVD (MOCVD),[2,15−19] atomic layer deposition (ALD),[20−25] and physical vapor deposition (sputtering)[26−31] provide other approaches that are also potentially more compatible with conventional, industrial semiconductor fabrication. Among these, ALD and sputtering have not been as commonly studied as (MO)CVD, and more work is needed to understand their limitations and improve their quality.[22,32−37]

In this study, we examine and compare the quality of few-layer (2−5L) $MoS_2$ films prepared by ALD and radio frequency (RF) sputtering, as-grown and with an annealing step hypothesized to improve film quality. We analyze the films using Raman spectroscopy, X-ray photoelectron spectroscopy (XPS), transmission electron microscopy (TEM), atomic force microscopy (AFM), as well as electrical device characterization and uncover certain correlations between Raman or AFM features and the electrical behavior (i.e., transistor mobility and on/off current ratio) of the films. We expect that the metrology explored and the insights obtained in this work will aid in reducing future research and development timelines for implementing TMDs in electronic applications.

## RESULTS AND DISCUSSION

**Initial Material Study.** The details of the $MoS_2$ ALD process have been described in previous work.[38] In brief, these films are prepared at a BEOL-compatible temperature of 500

Received: March 4, 2025
Revised: June 16, 2025
Accepted: June 16, 2025
Published: August 8, 2025




https://doi.org/10.1021/acsami.5c04483
*ACS Appl. Mater. Interfaces* 2025, 17, 47347−47354

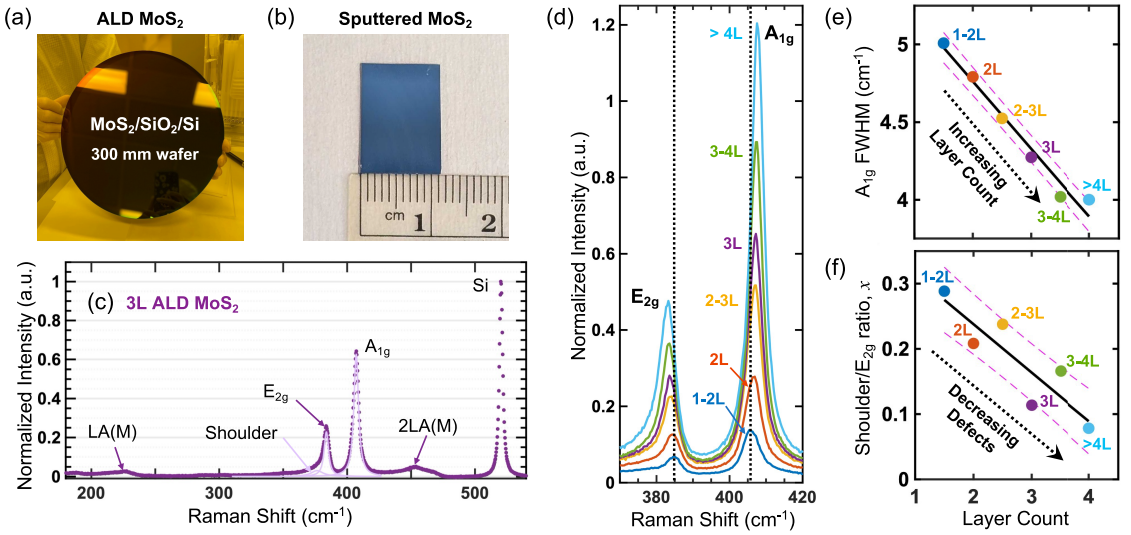


**Figure 1.** (a) Photograph of 300 mm Si wafer covered by ALD $MoS_2$ on $SiO_2$. (b) Photograph of $SiO_2$/Si substrates coated with RF-sputtered $MoS_2$. (c) Measured Raman spectra on 3-layer (3L) ALD $MoS_2$ (symbols) with peak fits (lines), normalized by the Si substrate peak at 520 $cm^{-1}$. (d) Raman spectra of ALD films of various thickness normalized by the Si substrate peak (not shown). Vertical dotted lines mark the $E_{2g}$ and $A_{1g}$ positions expected of monolayer films. (e) Correlation between Raman $A_{1g}$ peak full width at half-maximum (FWHM) and thickness of ALD-$MoS_2$ films. (f) Correlation between Raman shoulder/$E_{2g}$ intensity ratio ($x$) and thickness of ALD-$MoS_2$ films. Solid black lines are linear fits to the experimental data points. Pink dashed lines mark ± one standard deviation (0.09 in (e) and 0.04 in (f)) bounds of the fits.

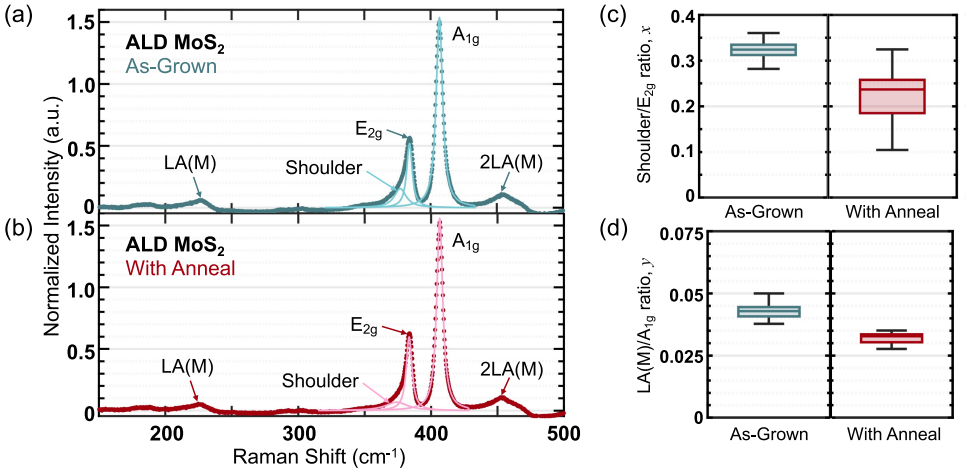


**Figure 2.** Raman analysis of 3−4L thick ALD $MoS_2$ films. (a) As-deposited and (b) post-anneal, at 900 °C for 1 min. Symbols mark experimental data, lines are fits, after a linear background subtraction. (c) Ratio of shoulder-to-$E_{2g}$ peak intensity, decreasing from 0.325 ± 0.031 (as-grown) to 0.230 ± 0.068 (after anneal). (d) Ratio of LA(M)-to-$A_{1g}$ peak intensity, decreasing from 0.043 ± 0.003 (as-grown) to 0.032 ± 0.002 (after anneal). Each box plot represents 75 point spectra, taken over three regions of 5 × 5 points each, with 1 $\mu$m point spacing. All data were taken at room temperature, and peak intensities are normalized to the Si peak.

°C, in an Ar atmosphere, onto 96 nm thermally grown $SiO_2$ on 300 mm (12 in.) Si wafers (Figure 1a). Our RF-sputtered $MoS_2$ films were prepared on similar substrates, but with lateral dimensions of a few centimeters (Figure 1b), also at the same deposition temperature of 500 °C. Sputtering was carried out with 10 sccm Ar, 12 W RF power, and a pressure of 2 mTorr, from a bulk $MoS_2$ target of 2-in. diameter. The size of the target used and the deposition chamber size limit our sputtered film substrate size here, but this can be easily overcome in industrial wafer-scale sputter processes.

To check and compare the optical quality of the films, we first employ Raman spectroscopy, which can nondestructively probe defects, doping, and strain in $MoS_2$[39,40] (see the Experimental Section for details on setup). The laser power used was sufficiently low to avoid heating damage of the $MoS_2$ films,[41] but high enough for a good signal-to-noise ratio (Figure 1c). The key Raman peaks were fit with a MATLAB script using a Voigt shape with a fixed Gaussian contribution to most accurately capture the line shape.[42−44] The Gaussian component is due to instrument-related broadening, with a full width at half-maximum (FWHM) of 1.31 $cm^{-1}$, estimated using the 277 $cm^{-1}$ peak from a neon lamp, and additional details about fitting are provided in Supporting Information Figures S1 and S2. The Lorentzian FWHM of each spectrum, which corresponds to the sample's intrinsic FWHM, was then fit systematically over enough trials to converge to the lowest error between the fitted spectra and raw data.


https://doi.org/10.1021/acsami.5c04483
ACS Appl. Mater. Interfaces 2025, 17, 47347−47354

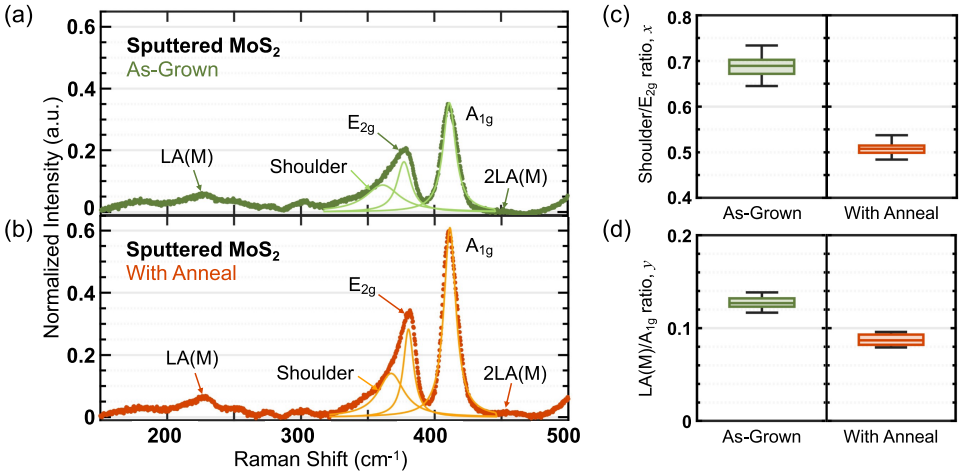


**Figure 3.** Raman analysis of 3−4L thick RF-sputtered $MoS_2$ films. (a) As-deposited and (b) post-anneal, at 900 °C for 1 min. Symbols mark experimental data; lines are fits, after a linear background subtraction. (c) Ratio of shoulder-to-$E_{2g}$ peak intensity decreased from 0.687 ± 0.022 (as-grown) to 0.507 ± 0.012 (annealed). (d) Ratio of LA(M)-to-$A_{1g}$ peak intensity, decreasing from 0.128 ± 0.005 (as-grown) to 0.087 ± 0.007 (annealed). Each box plot represents 50 point spectra, taken over two regions of 5 × 5 points each, with 1 $\mu$m point spacing. All data were taken at room temperature and peak intensities are normalized to the Si peak.

The spectra for different layer thicknesses of ALD $MoS_2$ are shown in Figure 1d. Thicker films have higher peak intensity with red-shifting of the in-plane $E_{2g}$ Raman mode and blue-shifting of the out-of-plane $A_{1g}$ mode, as expected. The blue shift of the $A_{1g}$ mode from monolayer to bulk has been attributed to phonon stiffening with thickness, while the $E_{2g}$ mode red-shift with thickness has been attributed to long-range Columbic interactions.[45,46] Importantly, we find that the FWHM of the $A_{1g}$ peak decreases with increasing layer count, as summarized in Figure 1e. Decreased FWHM for the first-order peaks is often used to indicate higher-quality films,[37,47] although we find that this metric is not sufficiently clear, by itself, for these nanocrystalline films. The improved film quality of the thicker films is also confirmed when the shoulder-to-$E_{2g}$ intensity ratio, $x$, is plotted in Figure 1f. This metric estimates the $MoS_2$ sample quality by relying on defect-activated phonon modes which make up the "left shoulder" of the $E_{2g}$ peak, with a lower ratio signifying lower defect density.[39,40,47] Supporting Information Figure S3 plots a similar trend using the LA(M)/$A_{1g}$ ratio, which can also estimate the defectivity of $MoS_2$.[39] From these results, we conclude that the material quality is relatively improved for the thicker $MoS_2$ films due to the additional thermal annealing and time spent in the ALD chamber.

**Effect of Thermal Annealing on Material Quality.** To investigate the effect of annealing as it relates to changing material quality and variability, several Raman maps were taken on both types of films (ALD and sputtered) as-grown and with an additional thermal annealing of 900 °C for 1 min in an inert $N_2$ environment at 10 Torr pressure, in a rapid thermal processing chamber. The spectra were collected with a spot size of 0.5 $\mu$m, in 5 $\mu$m by 5 $\mu$m maps with 1 $\mu$m steps between each point, resulting in 25 spectra per measurement. Each sample was measured a minimum of two times to account for potential variability across the films.

Using the fitting approach described earlier, we extracted intensities and FWHMs for the three main features of interest: the $E_{2g}$ shoulder, $E_{2g}$, and $A_{1g}$, as shown in Figure 2a,b. Figure 2c,d summarizes the evolution of the shoulder-to-$E_{2g}$ ratio and the LA(M)-to-$A_{1g}$ ratio for the as-grown ALD $MoS_2$ films and after rapid thermal annealing. These films have an average shoulder-to-$E_{2g}$ ratio of 0.325 ± 0.031 as-grown and 0.230 ± 0.068 after the annealing. This decrease in ratio suggests a lower defect density post annealing, which matches well with other demonstrations of annealing in the literature.[26,48] A similar trend is seen from the decrease in LA(M)-to-$A_{1g}$ ratio in Figure 2d, but we find that the changes are more difficult to discern from the $A_{1g}$ and $E_{2g}$ FWHMs (Supporting Information Figures S4a and S5a).

Similarly, we analyzed the RF-sputtered $MoS_2$ films as-grown and with the same thermal annealing step. Relative to the Si substrate peak intensity (at 520 $cm^{-1}$), the sputtered film has a lower intensity and broader FWHM for the $A_{1g}$ peak (Figure 3a,b, as-grown and with anneal) compared to the ALD film (Figure 2a,b, as-grown and with anneal). This is consistent with the higher-quality layers present in the ALD film, as we will see from high-resolution TEM analysis below. Overall, the sputtered $MoS_2$ films have lower quality than the ALD films, both as-grown and after anneal, as seen from all their Raman metrics. However, the sputtered $MoS_2$ films display more obvious improvement after thermal annealing, with Figure 3c showing a decrease of average shoulder-to-$E_{2g}$ intensity ratio from 0.687 ± 0.022 to 0.507 ± 0.012, as-grown and with annealing, respectively. The LA(M)-to-$A_{1g}$ peak ratio (Figure 3d) as well as the $A_{1g}$ and $E_{2g}$ FWHM of the sputtered $MoS_2$ film (Supporting Information Figures S4b and S5b) similarly show more dramatic improvement with annealing. This indicates that the $A_{1g}$ and $E_{2g}$ FWHMs are reasonable gauges for changes in higher-defectivity films (sputtered) but the analysis of lower-defectivity films (ALD) requires additional Raman insights, such as the peak ratios described above.

To further investigate the nature of the two types of films, we carried out cross-sectional TEM with energy-dispersive X-ray spectroscopy (EDX), as well as surface characterization by AFM, as shown in Figure 4 (see the Experimental Section for details on TEM setup). The sample cross-sections for TEM were prepared using a focused ion beam in a scanning electron microscope (FIB-SEM) and capped with carbon-based epoxy prior to milling, as seen in Figure 4a,e. EDX analysis in Figure 4b,f confirms the expected elemental composition. The ALD


https://doi.org/10.1021/acsami.5c04483
ACS Appl. Mater. Interfaces 2025, 17, 47347−47354

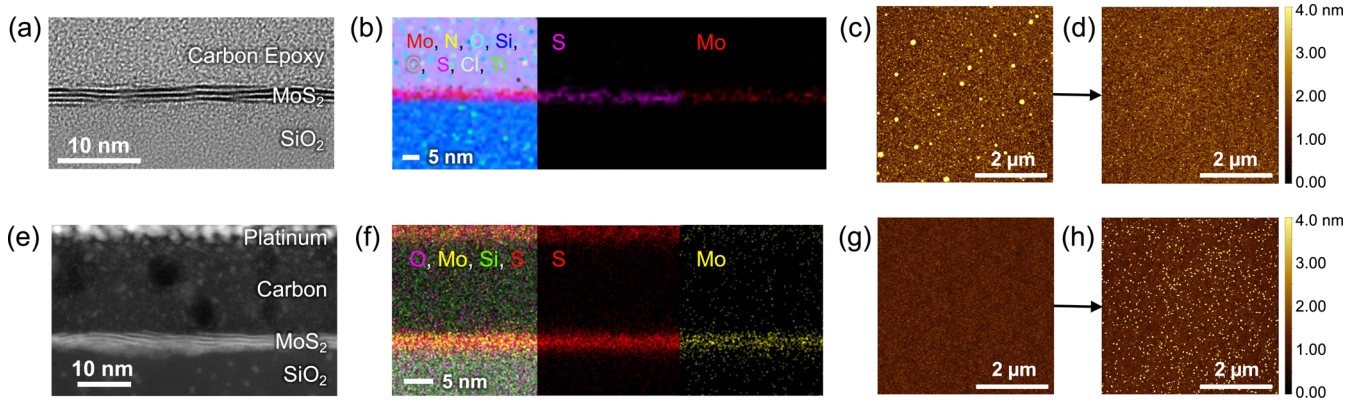


**Figure 4.** (a) Cross-sectional TEM image and (b) TEM-EDX elemental analysis of ALD $MoS_2$ film as-grown. (c) AFM scan of ALD $MoS_2$ film as-grown and (d) with annealing showed decreased surface roughness. (e) Cross-sectional STEM image and (f) TEM-EDX elemental analysis of as-grown RF-sputtered $MoS_2$ film. (g) AFM scan of RF-sputtered $MoS_2$ film as-grown and (h) with annealing showed increased surface roughness.

film cross section in Figure 4a shows a film thickness of ∼2.1 nm, with 3 to 4 atomic layers of $MoS_2$. The sputtered film cross section in Figure 4e shows between 2 and 4 layers of $MoS_2$, from bright contrast Mo−Mo planes, and ∼2.9 nm estimated film thickness. It is difficult to discern individual defects from the TEM cross-sections; however, in the sputtered $MoS_2$ film we observe inconsistent amounts of an amorphous oxide layer at the substrate (bottom) interface. The presence of amorphous oxides (e.g., $MoO_x$) in the sputtered $MoS_2$ films is consistent with their XPS analysis, as shown in Supporting Information Figure S7.

Interestingly, we observed that the rapid thermal annealing step had different effects on the surface roughness of ALD vs sputtered $MoS_2$ films (see the Experimental Section for details on AFM setup). The surface of the ALD films as-grown (Figure 4c) displays several large regions over 4 nm tall, but with the annealing (Figure 4d), these regions largely disappear, resulting in a more uniform film, consistent with the result of similar anneals in the literature.[48] The sputtered films tell a different story. Figure 4g shows that the sputtered $MoS_2$ films start out more uniform and flatter, with a root-mean-square (RMS) surface roughness of 276.8 pm. With annealing, the RMS surface roughness increases to 759.4 pm (Figure 4h), due to the appearance of small speckles scattered across the film. XPS measurements, provided in Supporting Information Figures S6 and S7, suggest that the overall stoichiometry remains relatively unchanged as-grown and with annealing, minimizing the possibility of oxidation being the culprit. However, previous studies[49−53] have suggested that such vertical domains can be produced, resulting in a film that was discontinuous laterally. Vertical domains are postulated to derive from $MoS_2$ islands, which evolve into vertical domains owing to competing defect and strain energies.[50,54]

To evaluate the electrical characteristics of these films, we fabricated back-gated field-effect transistors (FETs), with the schematic displayed in Figure 5a (see the Experimental Section for device fabrication details). The devices are placed in a vacuum probe station (∼$10^{-5}$ Torr) and annealed at 250 °C for 2 h, to remove adsorbates from the channel and to improve the contacts.[1] We measured the drain current $I_D$ vs back-gate voltage $V_{GS}$, at $V_{DS}$ = 0.1 V, without breaking vacuum after the samples cooled down to room temperature, as illustrated in Figure 5b−d. Using transfer length method (TLM)[55] analysis, we estimated the effective $MoS_2$ channel mobility from the slope of the total device resistance (at a fixed overdrive voltage[1]) vs channel length, as shown in Supporting Information Figure S8. We electrically tested TLM structures for each film (with 6 channel lengths, totaling 30 devices), which were fabricated and measured across 1 × 1 $cm^2$ chips. We extract the mobility from each individual TLM structure, and then we calculate the mean and standard deviation across these structures, as marked by the error bars in Figure 5e,f.

For the shortest ALD $MoS_2$ devices, we observe a nearly 4× increase in maximum current density with the annealing step, as shown in Figure 5b,c. Moreover, the current ratio $I_{on}/I_{off}$ increases by an order of magnitude, from ∼$10^3$ to ∼$10^4$. The hysteresis also improves, and together, these observations suggest a reduction of the number of defects and traps in the ALD films with the annealing step. On the other hand, the sputtered films display an order of magnitude lower current and effective mobility (than the ALD films) as-grown (Figure 5d−f), and their modest $I_{on}/I_{off}$ ratio is comparable to previous reports for sputtered $MoS_2$ films of similar thickness.[56] However, all sputtered $MoS_2$ films appeared to be open-circuit after the thermal annealing, and this degradation occurred likely due to vertical domain formation[50] and resulting discontinuity of sputtered $MoS_2$ films revealed in the AFM surface analysis (Figure 4h). The effective mobility from TLM measurements of these films is summarized in Figure 5e,f. The mobility was estimated to be 0.44 ± 0.09 $cm^2$ $V^{-1}$ $s^{-1}$ at room temperature in the ALD $MoS_2$ films with the annealing step, and the mobility (in general) is observed to scale inversely with the shoulder-to-$E_{2g}$ and the LA(M)-to-$A_{1g}$ intensity ratios, as expected.

To compare the films examined here with similar types of films reported in the literature, we extract the devices' transfer characteristics at $V_{DS}$ = 1 V (see Supporting Information Figure S9) and report a comprehensive benchmarking table including optical and electrical properties in Supporting Information Table S1 for ALD $MoS_2$ films and Table S2 for sputtered $MoS_2$ films.

## CONCLUSIONS

We have evaluated and compared few-layer $MoS_2$ films produced by two large-area synthesis methods (ALD and sputtering) through optical, topographical, X-ray, transmission electron microscopy, and electrical device measurements. The ALD films, in general, have better Raman features (e.g., lower shoulder-to-$E_{2g}$ and LA(M)-to-$A_{1g}$ intensity ratios, as well as lower $E_{2g}$ and $A_{1g}$ FWHMs), higher transistor current on/off


https://doi.org/10.1021/acsami.5c04483
ACS Appl. Mater. Interfaces 2025, 17, 47347−47354

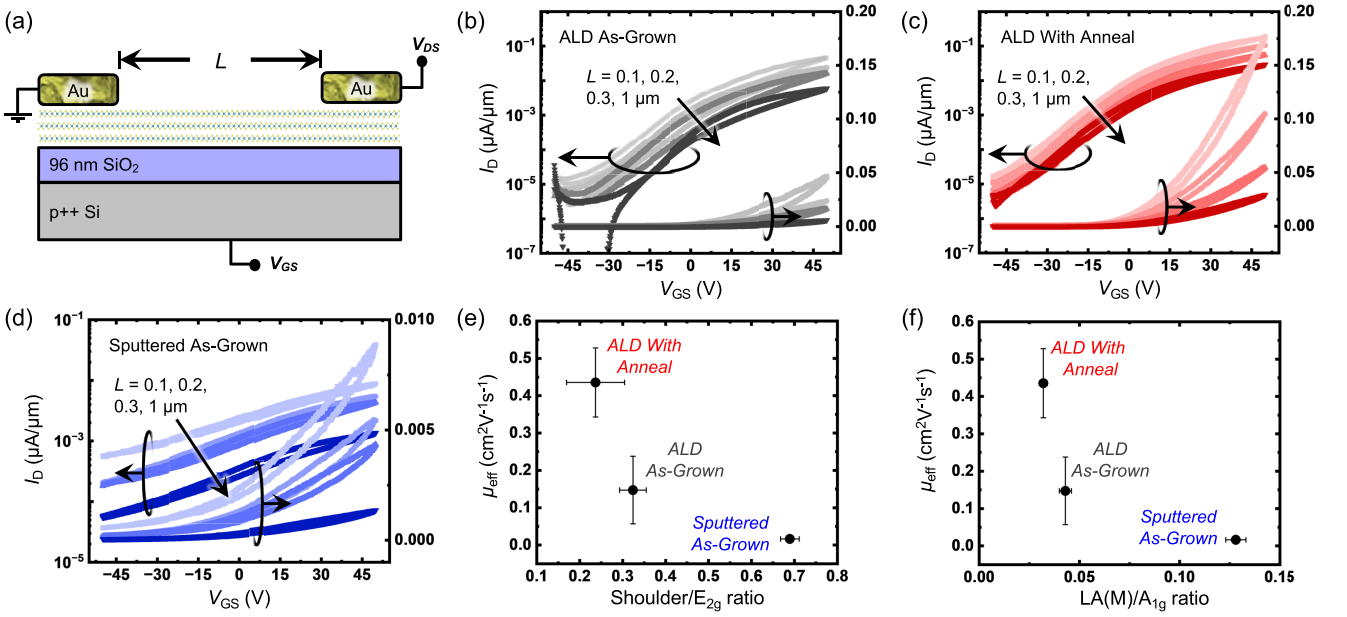


**Figure 5.** (a) Cross-sectional schematic of back-gated transistors used to estimate electron mobility in our ALD and sputtered $MoS_2$ films. (b) Measured transfer characteristics ($I_D$ vs $V_{GS}$) of ALD $MoS_2$ as-grown and (c) with annealing. (d) Measured $I_D$ vs $V_{GS}$ of RF-sputtered $MoS_2$ transistors as-grown. For (b–d), data are shown on log (left) and linear (right) axes, from four channel lengths, as labeled; forward and backward $V_{GS}$ sweeps reveal some clockwise hysteresis and all transfer characteristics are with $V_{DS}$ = 0.1 V. (e) Relationship between estimated $MoS_2$ mobility and Raman shoulder-to-$E_{2g}$ intensity ratio of 5 devices for each film. Error bars represent standard deviations across the measured data. (f) Relationship between estimated $MoS_2$ mobility and Raman LA(M)-to-$A_{1g}$ intensity ratio across all measured devices. Sputtered film data with annealing are not shown, as they were all open-circuit.

ratio, as well as higher mobility, and these metrics improve with rapid thermal annealing. In contrast, the sputtered films have higher surface roughness with annealing, and their electrical behavior degrades. This does not necessarily mean that one must always choose ALD over sputtered films, but the present study does provide a snapshot of how these compare currently, which is important for future improvements in both types of films. In particular, the observed correlation between Raman features and the electrical quality of the films suggests that such optical measurements can be used to rapidly screen the quality of 2D material layers in the future, while their synthesis is optimized, without having to rely on more time-consuming device fabrication and electrical device measurements. Besides improving the synthesis process, future work must also investigate different industry-compatible annealing conditions that improve film quality and reduce defects that may inadvertently form during synthesis.

## EXPERIMENTAL SECTION

**Fabrication of TLM Devices.** The $MoS_2$ films were directly deposited (by ALD or sputtering) onto 96 nm $SiO_2$ on $p^{++}$ Si, which also serves as a back-gate. The films used for electrical characterization are from the same deposition process as those used for TEM measurements. All device lithography steps were carried out on a Raith EBPG 5200+, forming 2 $\mu$m wide channels, patterned with $XeF_2$ etch, and source/drain contacts consisting of 50 nm thick Au, without an adhesion layer.[1] Devices were made as part of transfer length method (TLM) structures[55] with varying channel lengths from 0.1 to 1 $\mu$m.

**Materials Characterization.** All Raman spectra were acquired using a Horiba LabRAM instrument with a 100× short working distance objective, 532 nm excitation laser, 1800 lines/mm grating, 150 $\mu$m hole, and ~0.4 mW incident laser power. This setup enables a good resolution of 0.3 $cm^{-1}$ in each Raman spectrum. The ALD and RF-sputtered samples were separately imaged with probe-corrected Thermo Fisher Titan TEM microscopes at 200 and 300 kV, respectively. The ALD samples were imaged in high-resolution TEM (HRTEM) mode, while the sputtered samples were imaged in high-angle annular dark-field scanning TEM (HAADF-STEM) mode. Atomic force microscopy (AFM) imaging was conducted using a Bruker ICON AFM instrument with an NSC18/Pt tip in tapping mode. X-ray photoelectron spectroscopy (XPS) spectra were obtained from a VersaProbe 4 utilizing monochromatized Al(K$\alpha$) radiation (1486.6 eV) under high vacuum (~$10^{-7}$ Pa). The high-resolution Mo 3d, S 2p, and O 1s spectral regions were shifted to the reference hydrocarbon C 1s peak at 284.8 eV, as is the standard.

## ASSOCIATED CONTENT

### Supporting Information

The Supporting Information is available free of charge at https://pubs.acs.org/doi/10.1021/acsami.5c04483.

Neon lamp Raman measurements used to extract Gaussian component for Voigt peak fitting; comparison of Voigt peak fit to Gaussian/Lorentzian peak fit; other defect-related Raman metrics that were fit; XPS analysis of ALD and sputtered $MoS_2$ films before and after annealing for the Mo 3d, S 2p, and O 1s spectral regions; total resistance vs channel length extractions from the TLM device structures for ALD $MoS_2$ before and after annealing and sputtered $MoS_2$ before anneal; $I_D$ vs $V_{GS}$ measurements of 0.1 $\mu$m channel length at drain voltage $V_{DS}$ = 1 V; extensive electrical performance and Raman characteristics benchmarking table for both ALD and sputtered films in the literature (PDF)



https://doi.org/10.1021/acsami.5c04483
ACS Appl. Mater. Interfaces 2025, 17, 47347−47354

## AUTHOR INFORMATION


### Corresponding Author

**Eric Pop** − *Department of Electrical Engineering, Stanford University, Stanford, California 94305, United States; Precourt Institute for Energy and Department of Materials Science and Engineering, Stanford University, Stanford, California 94305, United States;* orcid.org/0000-0003-0436-8534; Email: epop@stanford.edu

### Authors

**Crystal Alicia Nattoo** − *Department of Electrical Engineering, Stanford University, Stanford, California 94305, United States;* orcid.org/0000-0001-9045-5575

**Tara Peña** − *Department of Electrical Engineering, Stanford University, Stanford, California 94305, United States*

**Koosha Nassiri Nazif** − *Department of Electrical Engineering, Stanford University, Stanford, California 94305, United States;* orcid.org/0000-0002-3991-6484

**Xiangjin Wu** − *Department of Electrical Engineering, Stanford University, Stanford, California 94305, United States*

**Sepideh Rahimisheikh** − *Department of Physics, University of Antwerp, Antwerpen 2000, Belgium*

**Giulio D'Acunto** − *Department of Chemical Engineering, Stanford University, Stanford, California 94305, United States;* orcid.org/0000-0002-0564-6906

**Stacey F. Bent** − *Department of Chemical Engineering and Precourt Institute for Energy, Stanford University, Stanford, California 94305, United States;* orcid.org/0000-0002-1084-5336

**Joke Hadermann** − *Department of Physics, University of Antwerp, Antwerpen 2000, Belgium;* orcid.org/0000-0002-1756-2566

Complete contact information is available at: https://pubs.acs.org/10.1021/acsami.5c04483


### Author Contributions

#C.A.N. and T.P. contributed equally to this work. C.A.N., K.N.N., and E.P. conceived the project. X.W. grew the sputtered $MoS_2$ films. C.A.N. and T.P. conducted Raman and X-ray photoelectron spectroscopy (XPS). G.D. and S.F.B. assisted with XPS analysis. T.P. completed atomic force microscopy, then fabricated and measured the device structures. S.R. performed transmission electron imaging for sputtered film, with guidance from J.H. All authors reviewed and gave approval to the final version of the manuscript.

### Notes

The authors declare no competing financial interest.

## ACKNOWLEDGMENTS

The authors thank Christina Newcomb for assistance with neon lamp spectral width calibration for Raman analysis and EMD Electronics for assistance with TEM on the ALD film. Part of this work was performed at the Stanford Nano Shared Facilities (SNSF), supported by the National Science Foundation (NSF) under award ECCS-2026822. C.A.N. acknowledges support from the NSF Graduate Fellowship Program. T.P. acknowledges support from the NSF MPS-Ascend Postdoctoral Fellowship. G.D. acknowledges support from Wallenberg Foundation Postdoctoral Scholarship Program KAW 2021.0342. C.A.N., K.N.N., and E.P. also acknowledge support from the Department of Energy Grant DE-AC02-06CH11357. X.W., T.P., and E.P. acknowledge partial support from PRISM and SUPREME, JUMP 2.0 Centers sponsored by the Semiconductor Research Corporation (SRC) and DARPA.

## REFERENCES


(1) English, C. D.; Shine, G.; Dorgan, V. E.; Saraswat, K. C.; Pop, E. Improved Contacts to $MoS_2$ Transistors by Ultra-High Vacuum Metal Deposition. *Nano Lett.* **2016**, *16* (6), 3824−3830.

(2) Chowdhury, S.; Roy, A.; Liu, C.; Alam, M. H.; Ghosh, R.; Chou, H.; Akinwande, D.; Banerjee, S. K. Two-Step Growth of Uniform Monolayer $MoS_2$ Nanosheets by Metal-Organic Chemical Vapor Deposition. *ACS Omega* **2021**, *6* (15), 10343−10351.

(3) Park, J. H.; Lu, A. Y.; Shen, P. C.; Shin, B. G.; Wang, H.; Mao, N.; Xu, R.; Jung, S. J.; Ham, D.; Kern, K.; et al. Synthesis of High-Performance Monolayer Molybdenum Disulfide at Low Temperature. *Small Methods* **2021**, *5* (6), No. 2000720.

(4) Park, Y. J.; Sharma, B. K.; Shinde, S. M.; Kim, M. S.; Jang, B.; Kim, J. H.; Ahn, J. H. All $MoS_2$-Based Large Area, Skin-Attachable Active-Matrix Tactile Sensor. *ACS Nano* **2019**, *13* (3), 3023−3030.

(5) Li, N.; Wang, Q. Q.; Shen, C.; Wei, Z.; Yu, H.; Zhao, J.; Lu, X. B.; Wang, G. L.; He, C. L.; Xie, L.; et al. Large-scale flexible and transparent electronics based on monolayer molybdenum disulfide field-effect transistors. *Nat. Electron.* **2020**, *3* (11), 711−717.

(6) Daus, A.; Vaziri, S.; Chen, V.; Köroglu, C.; Grady, R. W.; Bailey, C. S.; Lee, H. R.; Schauble, K.; Brenner, K.; Pop, E. High-performance flexible nanoscale transistors based on transition metal dichalcogenides. *Nat. Electron.* **2021**, *4* (7), 495−501.

(7) Shinde, S. M.; Das, T.; Hoang, A. T.; Sharma, B. K.; Chen, X.; Ahn, J. H. Surface-Functionalization-Mediated Direct Transfer of Molybdenum Disulfide for Large-Area Flexible Devices. *Adv. Funct. Mater.* **2018**, *28*, No. 1706231.

(8) Hoang, A. T.; Hu, L.; Katiyar, A. K.; Ahn, J.-H. Two-dimensional layered materials and heterostructures for flexible electronics. *Matter* **2022**, *5* (12), 4116−4132.

(9) Hoang, A. T.; Hu, L.; Kim, B. J.; Van, T. T. N.; Park, K. D.; Jeong, Y.; Lee, K.; Ji, S.; Hong, J.; Katiyar, A. K.; et al. Low-temperature growth of $MoS_2$ on polymer and thin glass substrates for flexible electronics. *Nat. Nanotechnol.* **2023**, *18* (12), 1439−1447.

(10) Smithe, K. K. H.; Suryavanshi, S. V.; Rojo, M. M.; Tedjarati, A. D.; Pop, E. Low Variability in Synthetic Monolayer $MoS_2$ Devices. *ACS Nano* **2017**, *11* (8), 8456−8463.

(11) Smithe, K. K. H.; English, C. D.; Suryavanshi, S. V.; Pop, E. Intrinsic electrical transport and performance projections of synthetic monolayer $MoS_2$ devices. *2D Mater.* **2017**, *4* (1), No. 011009.

(12) Wu, X. Y.; Lin, D.; Cott, D.; De Marneffe, J. F.; Groven, B.; Sergeant, S.; Shi, Y. Y.; Smets, Q.; Sutar, S.; Asselberghs, I.; et al. In *ALD Encapsulation of CVD $WS_2$ for Stable and High-Performance FET Devices*, 2021 Electron Devices Technology and Manufacturing Conference (EDTM); IEEE, 2021; https://doi.org/10.1109/EDTM50988.2021.9420940.

(13) Zhang, Y.; Yao, Y.; Sendeku, M. G.; Yin, L.; Zhan, X.; Wang, F.; Wang, Z.; He, J. Recent Progress in CVD Growth of 2D Transition Metal Dichalcogenides and Related Heterostructures. *Adv. Mater.* **2019**, *31* (41), No. 1901694.

(14) Sousa, F. B.; Nadas, R.; Martins, R.; Barboza, A. P. M.; Soares, J. S.; Neves, B. R. A.; Silvestre, I.; Jorio, A.; Malard, L. M. Disentangling doping and strain effects at defects of grown $MoS_2$ monolayers with nano-optical spectroscopy. *Nanoscale* **2024**, *16* (27), 12923−12933.

(15) Cwik, S.; Mitoraj, D.; Reyes, O. M.; Rogalla, D.; Peeters, D.; Kim, J.; Schütz, H. M.; Bock, C.; Beranek, R.; Devi, A. Direct Growth of $MoS_2$ and $WS_2$ Layers by Metal Organic Chemical Vapor Deposition. *Adv. Mater. Interfaces* **2018**, *5* (16), No. 1800140.

(16) Cohen, A.; Patsha, A.; Mohapatra, P. K.; Kazes, M.; Ranganathan, K.; Houben, L.; Oron, D.; Ismach, A. Growth-Etch Metal-Organic Chemical Vapor Deposition Approach of $WS_2$ Atomic Layers. *ACS Nano* **2021**, *15* (1), 526−538.

(17) Mun, J.; Park, H.; Park, J.; Joung, D.; Lee, S. K.; Leem, J.; Myoung, J. M.; Park, J.; Jeong, S. H.; Chegal, W. C.; et al. High-Mobility $MoS_2$ Directly Grown on Polymer Substrate with Kinetics-Controlled Metal-Organic Chemical Vapor Deposition. *ACS Appl. Electron. Mater.* **2019**, *1* (4), 608−616.
(18) Wang, Z.; Tripathi, M.; Golsanamlou, Z.; Kumari, P.; Lovarelli, G.; Mazziotti, F.; Logoteta, D.; Fiori, G.; Sementa, L.; Marega, G. M.; et al. Substitutional p-Type Doping in $NbS_2$ -$MoS_2$ Lateral Heterostructures Grown by MOCVD. *Adv. Mater.* **2023**, *35* (14), No. 2209371.
(19) Gong, Y. Y.; Zhang, X. T.; Redwing, J. M.; Jackson, T. N. Thin Film Transistors Using Wafer-Scale Low-Temperature MOCVD $WSe_2$. *J. Electron. Mater.* **2016**, *45* (12), 6280−6284.
(20) Zhang, T.; Wang, Y.; Xu, J.; Chen, L.; Zhu, H.; Sun, Q.; Ding, S.; Zhang, D. W. High performance few-layer $MoS_2$ transistor arrays with wafer level homogeneity integrated by atomic layer deposition. *2D Mater.* **2018**, *5* (1), No. 015028.
(21) Shi, M. L.; Chen, L.; Zhang, T. B.; Xu, J.; Zhu, H.; Sun, Q. Q.; Zhang, D. W. Top-Down Integration of Molybdenum Disulfide Transistors with Wafer-Scale Uniformity and Layer Controllability. *Small* **2017**, *13* (35), No. 1603157.
(22) Tian, Z. L.; Zhao, D. H.; Liu, H.; Zhu, H.; Chen, L.; Sun, Q. Q.; Zhang, D. W. Optimization of Defects in Large-Area Synthetic $MoS_2$ Thin Films by $CS_2$ Treatment for Switching and Sensing Devices. *ACS Appl. Nano Mater.* **2019**, *2* (12), 7810−7818.
(23) Liu, H.; Chen, L.; Zhu, H.; Sun, Q. Q.; Ding, S. J.; Zhou, P.; Zhang, D. W. Atomic layer deposited 2D $MoS_2$ atomic crystals: from material to circuit. *Nano Res.* **2020**, *13* (6), 1644−1650.
(24) Aspiotis, N.; Morgan, K.; März, B.; Müller-Caspary, K.; Ebert, M.; Weatherby, E.; Light, M. E.; Huang, C. C.; Hewak, D. W.; Majumdar, S.; Zeimpekis, I. Large-area synthesis of high electrical performance $MoS_2$ by a commercially scalable atomic layer deposition process. *npj 2D Mater. Appl.* **2023**, *7* (1), No. 18.
(25) Jeon, W.; Cho, Y.; Jo, S.; Ahn, J. H.; Jeong, S. J. Wafer-Scale Synthesis of Reliable High-Mobility Molybdenum Disulfide Thin Films via Inhibitor-Utilizing Atomic Layer Deposition. *Adv. Mater.* **2017**, *29* (47), No. 1703031.
(26) Kitazawa, T.; Inaba, Y.; Yamashita, S.; Imai, S.; Kurohara, K.; Tatsumi, T.; Wakabayashi, H.; Tomiya, S. Impact of crystallinity on thermal conductivity of RF magnetron sputtered $MoS_2$ thin films. *Jpn. J. Appl. Phys.* **2024**, *63* (5), No. 055508.
(27) Wahid, S.; Daus, A.; Khan, A. I.; Chen, V.; Neilson, K. M.; Islam, M.; Chen, M. E.; Pop, E. Lateral electrical transport and field-effect characteristics of sputtered p-type chalcogenide thin films. *Appl. Phys. Lett.* **2021**, *119* (23), No. 232106.
(28) Gupta, D.; Chauhan, V.; Kumar, R. Sputter deposition of 2D $MoS_2$ thin films - A critical review from a surface and structural perspective. *Inorg. Chem. Commun.* **2022**, *144*, No. 109848.
(29) Park, H.; Liu, N.; Kim, B. H.; Kwon, S. H.; Baek, S.; Kim, S.; Lee, H. K.; Yoon, Y. J.; Kim, S. Exceptionally Uniform and Scalable Multilayer $MoS_2$ Phototransistor Array Based on Large-Scale $MoS_2$ Grown by RF Sputtering, Electron Beam Irradiation, and Sulfurization. *ACS Appl. Mater. Interfaces* **2020**, *12* (18), 20645−20652.
(30) Choudhary, N.; Park, J.; Hwang, J. Y.; Choi, W. Growth of large-scale and thickness-modulated $MoS_2$ nanosheets. *ACS Appl. Mater. Interfaces* **2014**, *6* (23), 21215−21222.
(31) Huang, J. H.; Chen, H. H.; Liu, P. S.; Lu, L. S.; Wu, C. T.; Chou, C. T.; Lee, Y. J.; Li, L. J.; Chang, W. H.; Hou, T. H. Large-area few-layer $MoS_2$ deposited by sputtering. *Mater. Res. Express* **2016**, *3* (6), No. 065007.
(32) Edelberg, D.; Rhodes, D.; Kerelsky, A.; Kim, B.; Wang, J.; Zangiabadi, A.; Kim, C.; Abhinandan, A.; Ardelean, J.; Scully, M.; et al. Approaching the Intrinsic Limit in Transition Metal Diselenides via Point Defect Control. *Nano Lett.* **2019**, *19* (7), 4371−4379.
(33) Tian, X.; Yan, X.; Varnavides, G.; Yuan, Y.; Kim, D. S.; Ciccarino, C. J.; Anikeeva, P.; Li, M. Y.; Li, L. J.; Narang, P.; et al. Capturing 3D atomic defects and phonon localization at the 2D heterostructure interface. *Sci. Adv.* **2021**, *7* (38), No. eabi6699.
(34) Wu, Z. T.; Luo, Z. Z.; Shen, Y. T.; Zhao, W. W.; Wang, W. H.; Nan, H. Y.; Guo, X. T.; Sun, L. T.; Wang, X. R.; You, Y. M.; Ni, Z. Defects as a factor limiting carrier mobility in $WSe_2$: A spectroscopic investigation. *Nano Res.* **2016**, *9* (12), 3622−3631.
(35) Zhang, X.; Xu, J.; Zhi, A.; Wang, J.; Wang, Y.; Zhu, W.; Han, X.; Tian, X.; Bai, X.; Sun, B.; et al. Low-Defect-Density Monolayer $MoS_2$ Wafer by Oxygen-Assisted Growth-Repair Strategy. *Adv. Sci.* **2024**, *11* (42), No. 2408640.
(36) Xiao, Z.; Guo, R.; Zhang, C.; Liu, Y. Point Defect Limited Carrier Mobility in 2D Transition Metal Dichalcogenides. *ACS Nano* **2024**, *18* (11), 8511−8516.
(37) Fang, L.; Chen, H.; Yuan, X.; Huang, H.; Chen, G.; Li, L.; Ding, J.; He, J.; Tao, S. Quick Optical Identification of the Defect Formation in Monolayer $WSe_2$ for Growth Optimization. *Nanoscale Res. Lett.* **2019**, *14* (1), No. 274.
(38) Ngo, T.; Zacatzi, A.; Tan, Y.; Lee, D.; Waknis, A.; Vu, N.; Kanjolia, R.; Moinpour, M.; Chen, Z. In *300mm Wafer-scale ALD-grown $MoS_2$*, 2024 IEEE International Interconnect Technology Conference (IITC); IEEE, 2024.
(39) Mignuzzi, S.; Pollard, A. J.; Bonini, N.; Brennan, B.; Gilmore, I. S.; Pimenta, M. A.; Richards, D.; Roy, D. Effect of disorder on Raman scattering of single-layer $MoS_2$. *Phys. Rev. B* **2015**, *91* (19), No. 195411.
(40) Shi, W.; Zhang, X.; Li, X.-L.; Qiao, X.-F.; Wu, J.-B.; Zhang, J.; Tan, P.-H. Phonon Confinement Effect in Two-dimensional Nano-crystallites of Monolayer $MoS_2$ to Probe Phonon Dispersion Trends Away from Brillouin-Zone Center. *Chin. Phys. Lett.* **2016**, *33* (5), No. 057801.
(41) Yalon, E.; Aslan, B.; Smithe, K. K. H.; McClellan, C. J.; Suryavanshi, S. V.; Xiong, F.; Sood, A.; Neumann, C. M.; Xu, X.; Goodson, K. E.; et al. Temperature-Dependent Thermal Boundary Conductance of Monolayer $MoS_2$ by Raman Thermometry. *ACS Appl. Mater. Interfaces* **2017**, *9* (49), 43013−43020.
(42) Zaghloul, M. R. On the calculation of the Voigt line profile: a single proper integral with a damped sine integrand. *Mon. Not. R. Astron. Soc.* **2007**, *375* (3), 1043−1048.
(43) Michail, A.; Delikoukos, N.; Parthenios, J.; Galiotis, C.; Papagelis, K. Optical detection of strain and doping inhomogeneities in single layer $MoS_2$. *Appl. Phys. Lett.* **2016**, *108* (17), No. 173102.
(44) Ulrich, C.; Anastassakis, E.; Syassen, K.; Debernardi, A.; Cardona, M. Lifetime of Phonons in Semiconductors under Pressure. *Phys. Rev. Lett.* **1997**, *78* (7), No. 1283.
(45) Lee, C.; Yan, H.; Brus, L. E.; Heinz, T. F.; Hone, J.; Ryu, S. Anomalous lattice vibrations of single- and few-layer $MoS_2$. *ACS Nano* **2010**, *4* (5), 2695−2700.
(46) Zhang, X.; Qiao, X. F.; Shi, W.; Wu, J. B.; Jiang, D. S.; Tan, P. H. Phonon and Raman scattering of two-dimensional transition metal dichalcogenides from monolayer, multilayer to bulk material. *Chem. Soc. Rev.* **2015**, *44* (9), 2757−2785.
(47) Dash, A. K.; Swaminathan, H.; Berger, E.; Mondal, M.; Lehenkari, T.; Prasad, P. R.; Watanabe, K.; Taniguchi, T.; Komsa, H.-P.; Singh, A. Evidence of defect formation in monolayer $MoS_2$ at ultralow accelerating voltage electron irradiation. *2D Mater.* **2023**, *10* (3), No. 035002.
(48) Wen, M.; Xu, J.; Liu, L.; Lai, P.-T.; Tang, W.-M. Improved Electrical Performance of Multilayer $MoS_2$ Transistor With $NH_3$-Annealed ALD HfTiO Gate Dielectric. *IEEE Trans. Electron Devices* **2017**, *64* (3), 1020−1025.
(49) Chen, G.; Lu, B.; Cui, X.; Xiao, J. Effects of Deposition and Annealing Temperature on the Structure and Optical Band Gap of $MoS_2$ Films. *Materials* **2020**, *13* (23), No. 5515.
(50) Wadhwa, R.; Thapa, S.; Deswal, S.; Kumar, P.; Kumar, M. Wafer-scale controlled growth of $MoS_2$ by magnetron sputtering: from in-plane to inter-connected vertically-aligned flakes. *J. Phys.: Condens. Matter* **2023**, *35* (12), No. 124002.
(51) Ohashi, T.; Suda, K.; Ishihara, S.; Sawamoto, N.; Yamaguchi, S.; Matsuura, K.; Kakushima, K.; Sugii, N.; Nishiyama, A.; Kataoka, Y.; et al. Multi-layered $MoS_2$ film formed by high-temperature


https://doi.org/10.1021/acsami.5c04483
ACS Appl. Mater. Interfaces 2025, 17, 47347−47354

sputtering for enhancement-mode nMOSFETs. *Jpn. J. Appl. Phys.* **2015**, *54* (4), No. 04DN08.
(52) Hussain, S.; Singh, J.; Vikraman, D.; Singh, A. K.; Iqbal, M. Z.; Khan, M. F.; Kumar, P.; Choi, D. C.; Song, W.; An, K. S.; et al. Large-area, continuous and high electrical performances of bilayer to few layers $MoS_2$ fabricated by RF sputtering via post-deposition annealing method. *Sci. Rep.* **2016**, *6*, No. 30791.
(53) Qi, M.; Xiao, J. R.; Gong, C. Y. Thermal annealing effects on the electrophysical characteristics of sputtered $MoS_2$ thin films by Hall effect measurements. *Semicond. Sci. Technol.* **2019**, *34* (4), No. 045017.
(54) Li, H.; Wu, H.; Yuan, S.; Qian, H. Synthesis and characterization of vertically standing $MoS_2$ nanosheets. *Sci. Rep.* **2016**, *6*, No. 21171.
(55) Schroder, D. K. *Semiconductor Material and Device Characterization*; Wiley, 2015.
(56) Matsuura, K.; Hamada, M.; Hamada, T.; Tanigawa, H.; Sakamoto, T.; Hori, A.; Muneta, I.; Kawanago, T.; Kakushima, K.; Tsutsui, K.; et al. Normally-off sputtered-$MoS_2$ nMISFETs with TiN top-gate electrode all defined by optical lithography for chip-level integration. *Jpn. J. Appl. Phys.* **2020**, *59* (8), No. 080906.

## NOTE ADDED AFTER ASAP PUBLICATION

This paper was published ASAP on August 8, 2025. A correction was made to the caption of Figure 5 and the paper was reposted on August 11, 2025.





https://doi.org/10.1021/acsami.5c04483
*ACS Appl. Mater. Interfaces* 2025, 17, 47347−47354

# Supporting Information

## Optoelectronic properties of atomic layer deposited and sputtered $MoS_2$ Films

Crystal Alicia Nattoo[1,†], Tara Peña[1,†], Koosha Nassiri Nazif[1], Xiangjin Wu[1], Sepideh Rahimisheikh[2], Giulio D'Acunto[3], Stacey F. Bent[3,4], Joke Hadermann[2], and Eric Pop[1,4,5,*]

*[1]Department of Electrical Engineering, Stanford University, Stanford, California 94305, USA*
*[2]Department of Physics, University of Antwerp, Antwerpen, 2000 Belgium*
*[3]Department of Chemical Engineering, Stanford University, Stanford, California 94305, USA*
*[4]Precourt Institute for Energy, Stanford University, Stanford, California 94305, USA*
*[5]Department of Materials Science and Engineering, Stanford University, Stanford, California 94305, USA*
*[†]These authors contributed equally to this work.*

*[*]Author to whom correspondence should be addressed: epop@stanford.edu*

## 1. Importance of using the Voigt Shape to Fit Raman Spectra

Due to the relative sharpness of the Raman features (few $cm^{-1}$) the intrinsic spectra of $MoS_2$ cannot be accurately captured without separating the extrinsic broadening caused by the optics of the Raman tool used for the measurement. To compare measurements taken on different tools, it is best to separate the Gaussian instrument broadening from the intrinsic Lorentzian linewidth.[1, 2] This can be done by measuring the spectra of a neon lamp within the typical measurement range, and then extracting the full-width half maximum (FWHM) from the neon peaks closest to the peaks of interest,[1] as shown in **Figure S1**. There is no standard method of choosing which neon peak to use so we used the 277.8 $cm^{-1}$ for this work as it was seemingly closer to our peaks of interest. An alternative fitting method, such as the commonly used Gaussian/Lorentzian blend, can lead to misleading trends due to additional fitting error, as shown in **Figure S2**.[3]

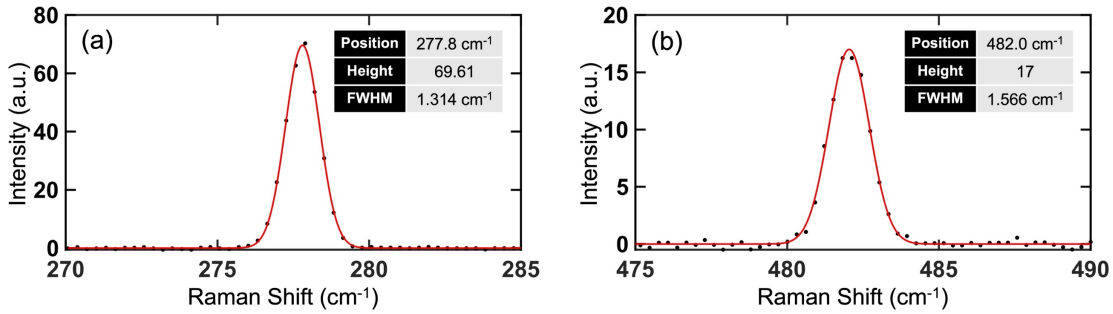


**Figure S1.** Neon lamp Raman spectra to extract instrument-related Gaussian broadening of our Horiba LabRAM. **(a)** FWHM of 1.314 $cm^{-1}$ for the peak at 277.8 $cm^{-1}$, which was used for all analyses. **(b)** FWHM of 1.566 $cm^{-1}$ for the peak at 482.0 $cm^{-1}$. Red line is fit of data after linear background subtraction and black dots are raw data points.

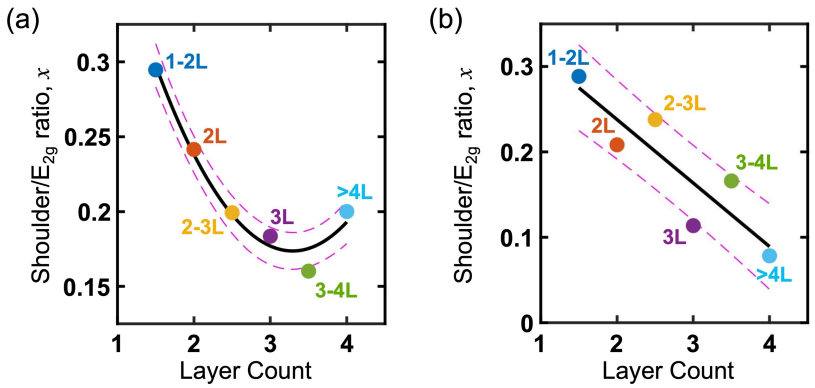


**Figure S2.** Difference in fitting of Raman shoulder-to-$E_{2g}$ intensity ratio vs. thickness of ALD-grown $MoS_2$ films. **(a)** Using 50:50 Gaussian/Lorentzian blend, which causes higher residual error, worsening the fit of the smaller shoulder peaks in the thicker films. **(b)** Results using Voigt fit, which accounts for the measured Gaussian contribution of the instrument, as implemented in our analysis in the main text. Solid black lines are fits to the experimental data points [linear fit in (b)]. Pink dashed lines represent plus/minus one standard deviation (±1 STD) bounds of the fits.

## 2. Other Defect-related Raman Metrics

Although other metrics have been used in the literature for atomic defect quantification, we have focused on the shoulder-to-$E_{2g}$ intensity ratio[4, 5] and LA(M)-to-$A_{1g}$ intensity ratio[6] in this work. Due to the higher defectivity of our ALD $MoS_2$, the LA(M)-to-$A_{1g}$ intensity ratio remains viable and displays the same trend of decreasing defects with decreasing layer count (**Figure S3**), as seen with the shoulder-to-$E_{2g}$ intensity ratio. This metric becomes limited when a material is monolayer and/or higher in quality, because in our experience the LA(M) vanishes before the $E_{2g}$ shoulder (in lower-defectivity samples).

For the same ALD and RF sputtered $MoS_2$ samples, as-grown and with anneal, we examined two additional defect-related metrics, the $A_{1g}$ peak FWHM and $E_{2g}$ peak FWHM (**Figures S4** and **S5**, respectively). Both of these FWHM metrics have been used to estimate the defectivity of $MoS_2$ in the literature, but both can be affected by strain and doping[1] (which can also be related to chalcogen vacancies, i.e. defects) making it more difficult to disentangle the impact of defects alone. Another factor that impacts the analysis is the nanocrystalline nature of both types of films, resulting in an abundance of grain boundaries.

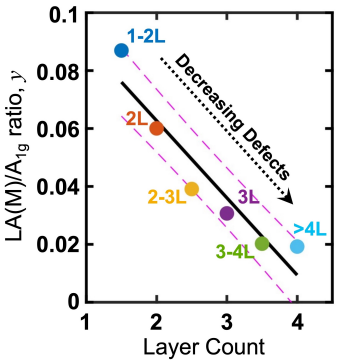


**Figure S3:** Correlation between Raman LA(M)-to-$A_{1g}$ intensity ratio and thickness of ALD-grown $MoS_2$ films. [For typical appearance of these peaks, see Figure 2(a, b) in the main text.] LA(M) is the mode around ~233 $cm^{-1}$. Solid black line is a linear fit to the experimental data points. Pink dashed lines represent plus/minus one standard deviation (±0.01) bounds of the fits.

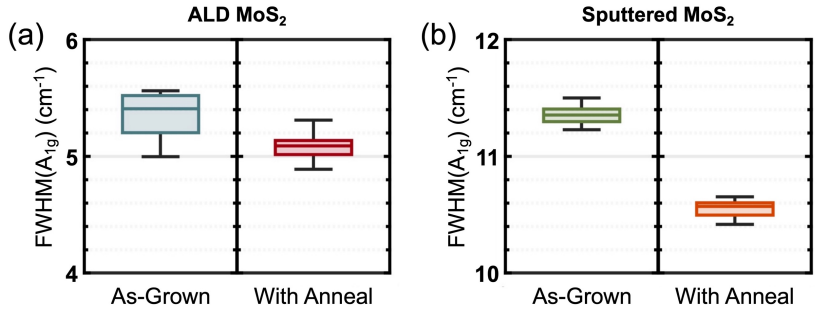


**Figure S4. (a)** Extracted $A_{1g}$ peak FWHM for 3-4L thick ALD $MoS_2$ films from Raman analysis, averaged over 75 spectra in a box plot. The $A_{1g}$ FWHM decrease slightly from 5.37 ± 0.16 $cm^{-1}$ (as-grown) to 5.08 ± 0.08 $cm^{-1}$ (annealed). **(b)** Extracted $A_{1g}$ peak FWHM for 3-4L thick RF sputtered $MoS_2$ films from Raman analysis, averaged over 50 spectra in a box plot. The $A_{1g}$ FWHM decrease from 11.36 ± 0.07 $cm^{-1}$ (as-grown) to 10.55 ± 0.07 $cm^{-1}$ (annealed). The spectra are taken over several regions of 5×5 points each, with 1 μm point spacing. All data were taken in room temperature ambient. Note the different vertical axis ranges.

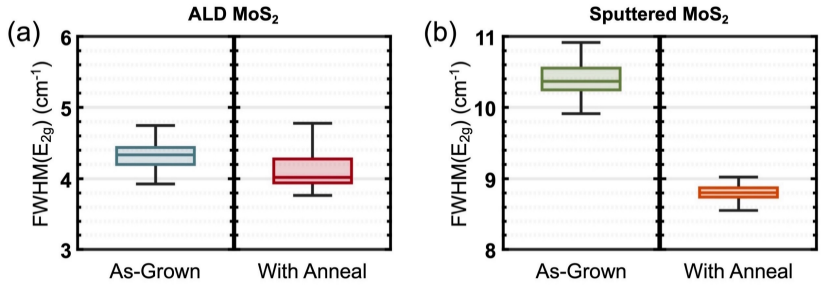


**Figure S5. (a)** Extracted $E_{2g}$ peak FWHM for 3-4L thick ALD $MoS_2$ films from Raman analysis, averaged over 75 spectra in a box plot. The $E_{2g}$ peak FWHMs remain effectively unchanged, 4.31 ± 0.20 $cm^{-1}$ (as-grown) and 4.13 ± 0.38 $cm^{-1}$ (annealed)]. **(b)** Extracted $E_{2g}$ peak FWHM for 3-4L thick RF sputtered $MoS_2$ films from Raman analysis, averaged over 50 spectra in a box plot. The $E_{2g}$ peak FWHMs decrease from 10.39 ± 0.22 $cm^{-1}$ (as-grown) to 8.81 ± 0.12 $cm^{-1}$ (annealed). The spectra are taken over several regions of 5×5 points each, with 1 μm point spacing. All data were taken in room temperature ambient. Note the different vertical axis ranges.

## 3. X-ray photoelectron spectroscopy (XPS) Analysis

To investigate changes in the chemical composition of these two $MoS_2$ films, X-ray photoelectron spectroscopy (XPS) spectra were obtained and then plotted together (**Figure S6**) to obtain insight into the few-layered $MoS_2$ before and after the rapid thermal anneal. [See Experimental Section in main text for details on the measurement setup.] Comparing all four films, there was little change in the S 2p spectral region, but there were some slight differences between the ALD and sputtered $MoS_2$ films in the Mo 3d region. The sputtered film had more chemical contribution from the Mo $3d_{3/2}$ energy and less contribution from the S 2s energy, suggesting these films are less stoichiometric than the ALD $MoS_2$ films.

The sputtered $MoS_2$ films also display a $MoO_x$ peak (**Figure S7**), which corroborates that these films are less stoichiometric and explains the amorphous oxide visualized by TEM (Figure 4e in the main text). This higher non-stoichiometry of the sputtered films is consistent with the Raman measurements [e.g., LA(M)-to-$A_{1g}$ intensity ratio and the FWHM of $E_{2g}$ and $A_{1g}$ have been shown to correlate with sulfur vacancies in monolayer $MoS_2$ films[6]] and with the worse electrical quality of the sputtered films (**Figure 5** in main text). However, in this work we found that the Raman measurements, if carefully interpreted, can provide more information than the XPS analysis. In other words, XPS can distinguish *between* ALD and sputtered films, but Raman analysis can discern more subtle differences before and after annealing the *same* film.

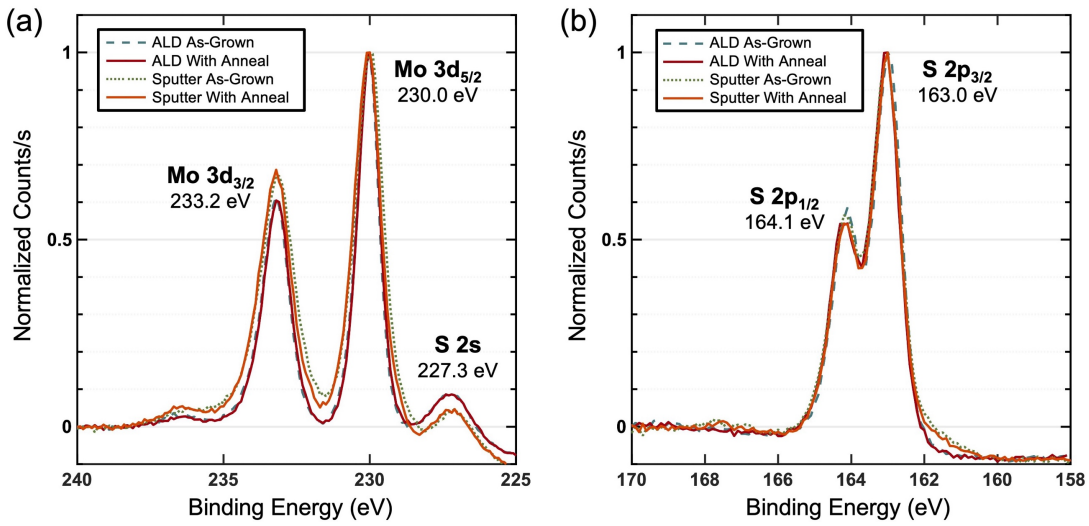


**Figure S6.** X-ray photoelectron spectroscopy (XPS) measurements of ALD $MoS_2$ and sputtered $MoS_2$ films. **(a)** Mo 3d region and **(b)** S 2p region. Measurement done with monochromatized Al(Kα) radiation (1486 eV) under high vacuum (~$10^{-7}$ Pa) with a resolution of 0.8 eV. Spectra normalized to highest intensity peak and background subtracted linearly. Dashed lines mark XPS spectra before anneal, solid lines are after the rapid anneal step. The sputtered films are relatively S-poor and Mo-rich compared to the ALD films.

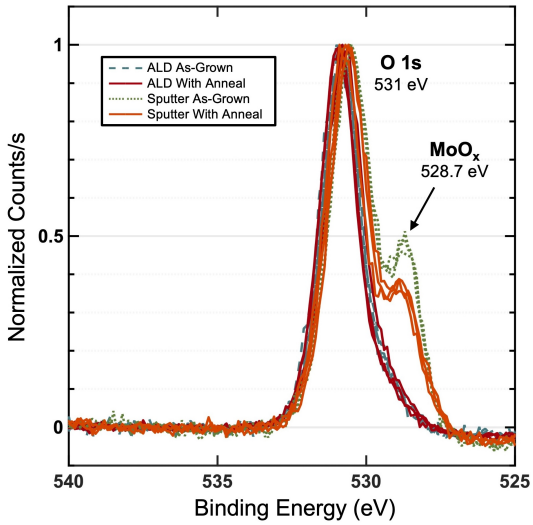


**Figure S7.** X-ray photoelectron spectroscopy (XPS) measurements of ALD $MoS_2$ and sputtered $MoS_2$ films for the O 1s region, with 3-4 scans each. Measurement done with monochromatized Al(Kα) radiation (1486 eV) under high vacuum (~$10^{-7}$ Pa) with a resolution of 0.8 eV. Spectra normalized to highest intensity peak and background subtracted linearly. Dashed lines mark XPS spectra before anneal, solid lines are after the rapid anneal step. We observe that only the sputtered $MoS_2$ films have a $MoO_x$ shoulder peak (as labeled), which is consistent with amorphous oxide layers visualized by TEM (Figure 4e in the main text).

## 4. Total Resistance vs. Channel Length from TLM Device Structures

The mobility estimates reported in **Figure 5** of the main text are from transfer length method (TLM) structures, where we extract the total resistance ($R_{tot}$) at a fixed gate overdrive voltage, vs. the channel length. The overdrive voltage is $V_{ov} = V_{GS} - V_T$, where $V_T$ is the threshold voltage determined using the constant-current method at 0.1 nA/μm.[7] The total resistance values displayed in **Figure S8** represent the mean values from 5 TLM structures. The TLM structures allow us to separate the contact resistance ($R_c$) and channel sheet resistance ($R_{sh}$) from $R_{tot} = 2R_c + R_{sh}L$, where $L$ is the channel length (contact separation). Fitting $R_{tot}$ vs. $L$ data to a linear equation provides an estimate of $2R_c$ from the vertical intercept and the effective mobility from the sheet resistance, as $\mu_{eff} = (qnR_{sh})^{-1}$, where $q$ is the elementary charge, $n \approx C_{ox}(V_{ov} - V_{DS}/2)/q$, and $C_{ox} \approx 38.9$ nF cm$^{-2}$ is the gate dielectric capacitance per unit area of 96 nm $SiO_2$. **Figure S9** plots the measured the drain current density $I_D$ vs. back-gate voltage $V_{GS}$, at $V_{DS} = 1$ V, to accompany the plots shown in **Figure 5b-d** to demonstrate that the same trend, improved current density correlating with the shoulder-to-$E_{2g}$ and the LA(M)-to-$A_{1g}$ intensity ratios, holds at higher drain voltage.

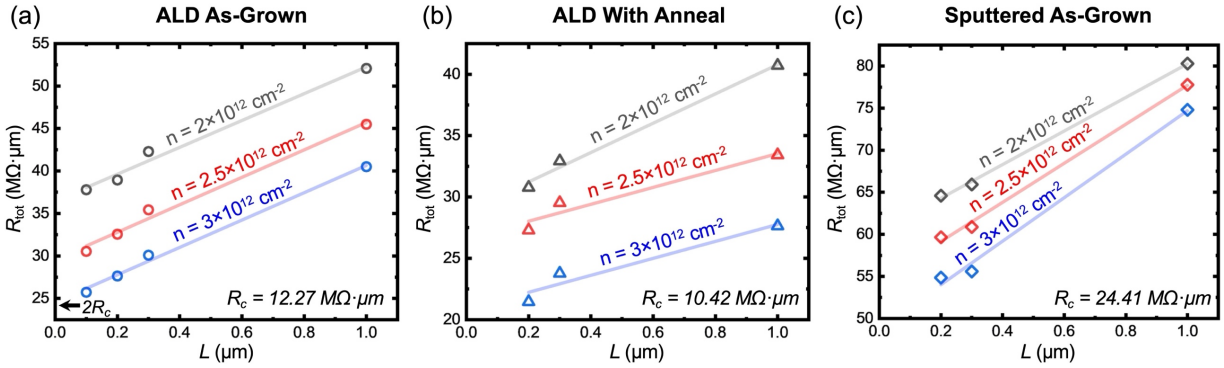


**Figure S8. (a)** Measured total resistance vs. channel length for ALD $MoS_2$ films as-grown and **(b)** with anneal. **(c)** Measured total resistance vs. channel length for RF sputtered $MoS_2$ transistors as-grown. All transfer characteristics are measured at room temperature in a vacuum probe station, with $V_{DS} = 0.1$ V.

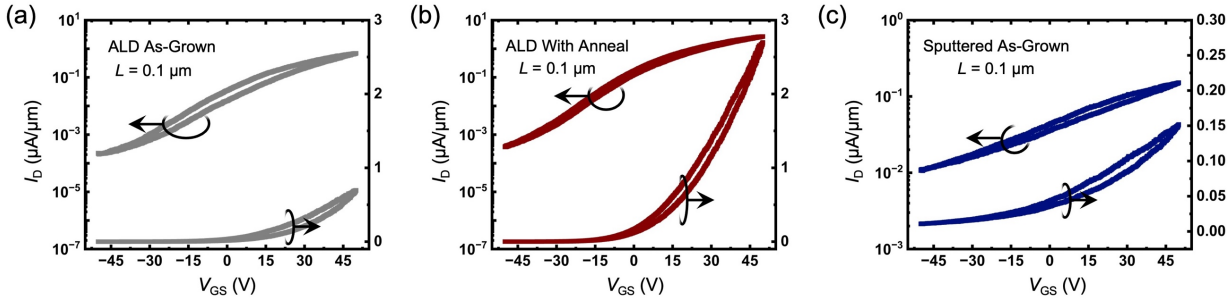


**Figure S9.** Measured transfer characteristics ($I_D$ vs. $V_{GS}$) of ALD $MoS_2$ **(a)** as-grown and **(b)** with anneal and **(c)** RF sputtered $MoS_2$ transistors as-grown. For (a-c), the data are shown on log (left) and linear (right) axes at a channel length $L = 0.1$ μm, as labeled; forward and backward $V_{GS}$ sweeps reveal some clockwise hysteresis and all transfer characteristics are with $V_{DS} = 1$ V.

## 5. Comparison with Previously Published ALD and Sputtered $MoS_2$ Characteristics

**Table S1:** Benchmarking table for work that investigates **atomic layer deposited (ALD)** $MoS_2$. "Temp." is the growth temperature, "$t_{film}$" is the film thickness, and "FWHM" are the full-width-half-maxima of the Raman peaks (extracted by us, through fitting, if they were not directly reported). If electrical transistor data were reported, we list them through $L$, the channel length, $I_{max}$, the maximum current density (at $V_{DS}$ = 0.1 V or 1 V and maximum $V_{GS}$), and $I_{max}/I_{min}$, the maximum on/off current ratio. We calculate and compare width-normalized current density (if the device width was available) rather than mobility, because mobility is prone to extraction uncertainty. **Note:** Some variation in FWHM may exist due to different Raman instruments, laser power, and spectrometer settings between measurements.

| Ref. # | Temp. (°C ) | ALD Precursor | Post-Deposition Anneal | $t_{film}$ (nm) | $E_{2g}$ FWHM ($cm^{-1}$) | $A_{1g}$ FWHM ($cm^{-1}$) | $L$ (µm) | $I_{max}$ (µA/µm) at $V_{DS}$ = 1 V (or at 0.1 V) | $I_{max}/I_{min}$ |
|---|---|---|---|---|---|---|---|---|---|
| **8** | 300 | molybdenum (V) chloride ($MoCl_5$) & hydrogen disulfide ($H_2S$) | 800°C in solid sulfur (SS) vapor for 30 min | 1.7 | 16 | 25 | / | / | / |
| | | | | 3.2 | 16 | 16 | / | / | / |
| | | | | 5.1 | 18 | 16 | / | / | / |
| **9** | 100 | $Mo(CO)_6$ & dimethyldisulfide ($CH_3SSCH_3$, DMDS) | / | 8.3 | 10 | 12 | / | / | / |
| | | | 900°C in Ar for 5 min | / | 9 | 9 | / | / | / |
| **10** | 350-450 | $MoCl_5$ & $H_2S$ | none | 1.3 | 10 | 9.5 | 20 | / | $2\times10^3$ |
| **11** | 200 | $Mo(CO)_6$ & $O_2$ plasma | 1) 200°C for 60 min in $H_2$ & Ar, 2) ramp up to 1000°C, 60 min in Ar & $H_2S$ | 1 | 4 | 5.2 | / | / | / |
| | | | | 1.6 | 4.5 | 5 | / | / | / |
| | | | | 2.3 | 5 | 4.5 | / | / | / |
| **12** | 500-900 | $MoCl_5$ & $H_2S$ | none | 0.8 | 7 | 5.6 | / | / | $10^8$ |
| **13** | 165 | $Mo(CO)_6$ & $H_2S$ | 500-900°C RTA in Ar or $H_2S$/Ar | 4.5 | 6.4 | 9 | / | / | / |
| **14** | 250 | $Mo(CO)_6$ & diethyl disulfide ($CH_3CH_2SS$-$CH_2CH_3$, DEDS) [pretreated wafer w/ ($CH_3CH_2SCH_2CH_3$), DES)] | 450°C RTA for 30s in Ar | 4.5 | 7 | 7 | 25 | 4 | $10^8$ |

| Ref. # | Temp. (°C ) | ALD Precursor | Post-Deposition Anneal | $t_{film}$ (nm) | $E_{2g}$ FWHM ($cm^{-1}$) | $A_{1g}$ FWHM ($cm^{-1}$) | $L$ (μm) | $I_{max}$ @ $V_{DS}$ = 1 V (or at 0.1 V) (μA/μm) | $I_{max}/I_{min}$ |
|---|---|---|---|---|---|---|---|---|---|
| **15** | 155 | $Mo(CO)_6$ & $O_2$ plasma | 1) 400°C for 20 min in Ar, 2) SS vapor at 500°C for 20 min 3) 900°C in same vapor for 20 min | 0.7 | 6 | 5.8 | 15 | (0.008 at 0.1 V) | $10^4$ |
| | | | | 1.39 | 6.5 | 6 | 25 | (0.0125 at 0.1 V) | $10^4$ |
| | | | | 2.74 | 7 | 6.5 | 25 | (0.05 at 0.1 V) | $5\times10^3$ |
| **16** | 150 | $Mo(CO)_6$ & hexamethyldisi-lathiane (HMDST) | 800°C for 20 min in SS vapor | 3 | 7.5 | 8.7 | 25 | 0.125 | $10^3$ |
| **17** | 375 | $MoCl_5$ & HMDST | 1) RTP at 800°C for 9 min, 2) $CS_2$ treatment 400°C for 1.7 hrs | 2.8 | 8 | 7 | 25 | 0.425 | 10 |
| **18** | 375 | $MoCl_5$ & HMDST | 800°C for 20 min in SS vapor | 5.6 | 4.2 | 3.6 | 40 | (0.00025 at 0.1 V) | $10^2$ |
| **19** | 300 | $MoCl_5$ & HMDST | 900°C in SS va-por for 45 min | 2.7 | 9 | 6.5 | 5 | 0.26 | $5\times10^2$ |
| **20** | 155 | $Mo(CO)_6$ and $O_2$ plasma | 1) 400°C for 20 min in Ar, 2) 500°C for 20 min in SS vapor, 3) 900°C in same vapor for 15 min | 2.85 | 6.4 | 7.5 | 5 | 0.1 | $10^3$ |
| **21** | 400 | $MoCl_5$ & HMDST | 800°C in SS vapor for 30 min | 2.96 | 5.6 | 5.7 | 5 | 4 | $10^3$ |
| **22** | 350 | $MoCl_5$ & HMDST | 900°C in SS vapor for 30 min-2hrs | 2.9 | 7 | 8 | 5 | 0.06 | $10^6$ |
| | | | | 2.9 | 7 | 8 | 5 | 0.188 | $10^6$ |
| **23** | 50 | $(NtBu)_2(NMe_2)_2Mo$ & $O_2$ plasma | 900°C in $H_2S$(10%)/Ar for 45 min | 1 | 5.2 | 5.5 | / | / | / |
| | | | | 4.5 | 5.4 | 5 | / | / | / |
| **24** | | | | 1.2 | 5 | 5.5 | / | / | / |
| | | | | 1.6 | 5.2 | 5.5 | / | / | / |

| Ref. # | Temp. (°C ) | ALD Precursor | Post-Deposition Anneal | $t_{film}$ (nm) | $E_{2g}$ FWHM ($cm^{-1}$) | $A_{1g}$ FWHM ($cm^{-1}$) | $L$ (μm) | $I_{max}$ @ $V_{DS}$ = 1 V (or at 0.1 V) (μA/μm) | $I_{max}/I_{min}$ |
|---|---|---|---|---|---|---|---|---|---|
| **25** | 250 | Bis(tert-butylimido) bis(dimethylamido) molybdenum [(NtBu)2(NMe2)2Mo] & $O_3$ | 900°C in SS vapor for 30 min | 2.2 | / | / | 1 | / | 40 |
| **26** | 250 | $[(NtBu)_2(NMe_2)_2Mo]$ & $O_3$ | 1) 550°C in $H_2S$/Ar, 2) 970°C in same atmosphere | 1.48 | 5.8 | 6.9 | 5 | (1.3 at 0.1 V) | $10^7$ |
| **This work** | 500 | commercial process with Ar carrier gas | none | 2.1 | 4.31 ± 0.20 | 5.37 ± 0.16 | 0.1 | 0.7 (0.06 at 0.1 V) | ~$10^3$ |
| **This work** | 500 | commercial process with Ar carrier gas | none | 2.1 | 4.31 ± 0.20 | 5.37 ± 0.16 | 1 | (0.006 at 0.1 V) | ~$10^3$ |
| **This work** | 500 | commercial process with Ar carrier gas | 900°C $N_2$ RTA anneal for 1 minute | 2.1 | 4.13 ± 0.38 | 5.08 ± 0.08 | 0.1 | 2.5 (0.175 at 0.1 V) | ~$10^4$ |
| **This work** | 500 | commercial process with Ar carrier gas | 900°C $N_2$ RTA anneal for 1 minute | 2.1 | 4.13 ± 0.38 | 5.08 ± 0.08 | 1 | (0.03 at 0.1 V) | ~$10^4$ |

**Table S2:** Benchmarking table for work that investigates **sputter-deposited** $MoS_2$. "Temp." is the growth temperature, "$t_{film}$" is the film thickness, and "FWHM" are the full-width-half-maxima of the Raman peaks (extracted by us, through fitting, if they were not directly reported). If electrical transistor data were reported, we list them through $L$, the channel length, $I_{max}$, the maximum current density (at $V_{DS}$ = 1 V and maximum $V_{GS}$), and $I_{max}/I_{min}$, the maximum on/off current ratio. We calculate and compare width-normalized current density (if the device width was available) rather than mobility, because mobility is prone to extraction uncertainty. **Note:** Some variation in FWHM may exist due to different Raman instruments, laser power, and spectrometer settings between measurements.

| Ref. # | Temp. (℃ ) | Sputter Target & RF or DC | Post-Deposition Anneal | $t_{film}$ (nm) | $E_{2g}$ FWHM ($cm^{-1}$) | $A_{1g}$ FWHM ($cm^{-1}$) | $L$ (μm) | $I_{max}$ @ $V_{DS}$ = 1 V (μA/μm) | $I_{max}/I_{min}$ |
|---|---|---|---|---|---|---|---|---|---|
| **27** | Room Temp (RT) | Mo (DC) | 600°C solid sulfur (SS) vapor | 4.18 | 8.9 | 9.8 | 10 | / | $1.56\times10^6$ |
| | | | | 6.44 | 12.2 | 14.4 | 10 | / | $5.7\times10^4$ |
| **28** | 300 | $MoS_2$ (RF) | none | 10 | 50.6 | 13.5 | / | / | / |
| **29** | RT | Mo (DC) | SS leaked into sputter chamber during growth | 0.7 | 6 | 4 | 100 | 0.002 | $10^3$ |
| **30** | 400 | $MoS_2$ (DC) | SS vapor, up to 1000°C | / | 5.5 | 5 | 50 | / | $10^4$ |
| | | | | 1.4 | 3 | 4 | 30 | / | $10^4$ |
| **31** | 500 | $MoS_2$ (RF) | 700°C in Ar / SS vapor | 1.4 | 13 | 9 | 2300 | 0.0115 | $10^4$ |
| | | | | 3.8 | 16 | 11 | 2300 | 0.052 | $4\times10^4$ |
| | | | | 6 | 13 | 9 | 2300 | 0.043 | $2\times10^3$ |
| **32** | 300 | $MoS_2$ (RF) | $(t\text{-}C_4H_9)_2S_2$ at ATM pressure | 6.81 | 10 | 10 | / | / | / |
| **33** | RT - 400 | $MoS_2$ (RF) | 485°C for 2 hrs in ambient | 2.5 | 8.5 | 7.4 | / | / | / |
| | | | | 20 | 16 | 13 | / | / | / |
| **34** | RT - 400 | $MoS_2$ (RF) | 250-1000°C Ar/SS vapor for 1 hr | 12 | 6 | 6 | / | / | / |
| **35** | 100-520 | $MoS_2$ (RF) | 600°C $N_2$ / SS vapor | / | 3 | 3.3 | / | / | / |
| | | | | / | 4.4 | 5.8 | / | / | / |
| **36** | RT | $MoS_2$ (RF) | 900°C in Ar for 40 min | 843 | 7 | 8.5 | / | / | / |
| **37** | RT | $MoS_2$ (RF) | 1) e-beam irradiation (EBI) treatment at 300W RF power for 1 min, 2) 950°C in $Ar/H_2S/H_2$ in CVD furnace for 1 hr | 2.2 | 7.8 | 8.5 | 3 | 0.001 | $1.3\times10^3$ |

| Ref. # | Temp. (°C ) | Sputter Target & RF or DC | Post-Deposition Anneal | $t_{film}$ (nm) | $E_{2g}$ FWHM ($cm^{-1}$) | $A_{1g}$ FWHM ($cm^{-1}$) | $L$ (μm) | $I_{max}$ @ $V_{DS}$ = 1 V (μA/μm) | $I_{max}/I_{min}$ |
|---|---|---|---|---|---|---|---|---|---|
| **38** | 300 | $MoS_2$ (RF) | none | / | 20 | 15 | 64 | / | $10^3$ |
| | | | | / | 18 | 17 | 64 | / | $10^3$ |
| **39** | RT | $MoS_2$ (RF) | 400°C & 700°C solid sulfur for 30 min | 180 | 6.4 | 10.1 | 200 | $1.74\times10^{-5}$ | 10 |
| **This work** | 500 | $MoS_2$ (RF) | none | 2.8 | 10.39 ± 0.22 | 11.36 ± 0.07 | 0.1 | 0.15 | 50 |
| **This work** | 500 | $MoS_2$ (RF) | 900°C $N_2$ RTA for 1 min | / | 8.81 ± 0.12 | 10.55 ± 0.07 | / | / | / |

## Supplementary References:


(1) Michail, A.; Delikoukos, N.; Parthenios, J.; Galiotis, C.; Papagelis, K. Optical detection of strain and doping inhomogeneities in single layer $MoS_2$. *Appl. Phys. Lett.* **2016**, *108* (17), 173102.
(2) Ulrich, C.; Anastassakis, E.; Syassen, K.; Debernardi, A.; Cardona, M. Lifetime of Phonons in Semiconductors under Pressure. *Phys. Rev. Lett.* **1997**, *78* (7), 1283-1286.
(3) Yuan, X.; Mayanovic, R. A. An Empirical Study on Raman Peak Fitting and Its Application to Raman Quantitative Research. *Appl. Spectrosc.* **2017**, *71* (10), 2325-2338.
(4) Shi, W.; Zhang, X.; Li, X.-L.; Qiao, X.-F.; Wu, J.-B.; Zhang, J.; Tan, P.-H. Phonon Confinement Effect in Two-dimensional Nanocrystallites of Monolayer $MoS_2$ to Probe Phonon Dispersion Trends Away from Brillouin-Zone Center. *Chin. Phys. Lett.* **2016**, *33* (5), 057801.
(5) Dash, A. K.; Swaminathan, H.; Berger, E.; Mondal, M.; Lehenkari, T.; Prasad, P. R.; Watanabe, K.; Taniguchi, T.; Komsa, H.-P.; Singh, A. Evidence of defect formation in monolayer $MoS_2$ at ultralow accelerating voltage electron irradiation. *2D Mater.* **2023**, *10* (3), 035002.
(6) Mignuzzi, S.; Pollard, A. J.; Bonini, N.; Brennan, B.; Gilmore, I. S.; Pimenta, M. A.; Richards, D.; Roy, D. Effect of disorder on Raman scattering of single-layer $MoS_2$. *Phys. Rev. B: Condens. Matter* **2015**, *91* (19), 195411.
(7) Ortiz-Conde, A.; García Sánchez, F. J.; Liou, J. J.; Cerdeira, A.; Estrada, M.; Yue, Y. A review of recent MOSFET threshold voltage extraction methods. *Microelectron. Reliab.* **2002**, *42*, 583-596.
(8) Tan, L. K.; Liu, B.; Teng, J. H.; Guo, S.; Low, H. Y.; Tan, H. R.; Chong, C. Y.; Yang, R. B.; Loh, K. P. Atomic layer deposition of a $MoS_2$ film. *Nanoscale* **2014**, *6* (18), 10584-10588.
(9) Jin, Z.; Shin, S.; Kwon, D. H.; Han, S. J.; Min, Y. S. Novel chemical route for atomic layer deposition of $MoS_2$ thin film on $SiO_2$/Si substrate. *Nanoscale* **2014**, *6* (23), 14453-14458.
(10) Browning, R.; Padigi, P.; Solanki, R.; Tweet, D. J.; Schuele, P.; Evans, D. Atomic layer deposition of $MoS_2$ thin films. *Mater. Res. Express* **2015**, *2* (3), 035006.
(11) Song, J. G.; Ryu, G. H.; Lee, S. J.; Sim, S.; Lee, C. W.; Choi, T.; Jung, H.; Kim, Y.; Lee, Z.; Myoung, J. M.; et al. Controllable synthesis of molybdenum tungsten disulfide alloy for vertically composition-controlled multilayer. *Nat Commun* **2015**, *6*, 7817.
(12) Kim, Y.; Song, J. G.; Park, Y. J.; Ryu, G. H.; Lee, S. J.; Kim, J. S.; Jeon, P. J.; Lee, C. W.; Woo, W. J.; Choi, T.; et al. Self-Limiting Layer Synthesis of Transition Metal Dichalcogenides. *Sci Rep* **2016**, *6*, 18754.
(13) Pyeon, J. J.; Kim, S. H.; Jeong, D. S.; Baek, S. H.; Kang, C. Y.; Kim, J. S.; Kim, S. K. Wafer-scale growth of $MoS_2$ thin films by atomic layer deposition. *Nanoscale* **2016**, *8* (20), 10792-10798.

(14) Jeon, W.; Cho, Y.; Jo, S.; Ahn, J. H.; Jeong, S. J. Wafer-Scale Synthesis of Reliable High-Mobility Molybdenum Disulfide Thin Films via Inhibitor-Utilizing Atomic Layer Deposition. *Adv. Mater.* **2017**, *29* (47), 1703031.
(15) Shi, M. L.; Chen, L.; Zhang, T. B.; Xu, J.; Zhu, H.; Sun, Q. Q.; Zhang, D. W. Top-Down Integration of Molybdenum Disulfide Transistors with Wafer-Scale Uniformity and Layer Controllability. *Small* **2017**, *13* (35), 1603157.
(16) Zhang, T.; Wang, Y.; Xu, J.; Chen, L.; Zhu, H.; Sun, Q.; Ding, S.; Zhang, D. W. High performance few-layer $MoS_2$ transistor arrays with wafer level homogeneity integrated by atomic layer deposition. *2D Mater.* **2018**, *5* (1), 015028.
(17) Tian, Z. L.; Zhao, D. H.; Liu, H.; Zhu, H.; Chen, L.; Sun, Q. Q.; Zhang, D. W. Optimization of Defects in Large-Area Synthetic $MoS_2$ Thin Films by $CS_2$ Treatment for Switching and Sensing Devices. *ACS Appl. Nano Mater.* **2019**, *2* (12), 7810-7818.
(18) Wang, Y.; Gu, Z.-H.; Liu, H.; Chen, L.; Liu, X.-k.; Min, L.; Li, Z.-w.; Zhu, H.; Sun, Q.-Q. Feasibility of Large-Scale $MoS_2$ Thin-Film Transistors on a GaN Substrate. *ACS Appl. Electron. Mater.* **2019**, *1* (8), 1418-1423.
(19) Zhang, T.; Liu, H.; Wang, Y.; Zhu, H.; Chen, L.; Sun, Q.; Zhang, D. W. Fast-Response Inverter Arrays Built on Wafer-Scale $MoS_2$ by Atomic Layer Deposition. *physica status solidi (RRL) – Rapid Research Letters* **2019**, *13* (7), 1900018.
(20) Chen, T.; Wang, Y.; Zhang, T.; Zhu, H.; Chen, L.; Sun, Q. Homogeneous dual-gate $MoS_2$ field-effect transistors integrated by atomic layer deposition-based film synthesis. *Journal of Materials Science: Materials in Electronics* **2020**, *31* (7), 5485-5491.
(21) Gu, Z.; Zhang, T.; Luo, J.; Wang, Y.; Liu, H.; Chen, L.; Liu, X.; Yu, W.; Zhu, H.; Sun, Q. Q.; et al. $MoS_2$-on-AlN Enables High-Performance $MoS_2$ Field-Effect Transistors through Strain Engineering. *ACS Appl Mater Interfaces* **2020**, *12* (49), 54972-54979.
(22) Liu, H.; Chen, L.; Zhu, H.; Sun, Q. Q.; Ding, S. J.; Zhou, P.; Zhang, D. W. Atomic layer deposited 2D $MoS_2$ atomic crystals: from material to circuit. *Nano Res.* **2020**, *13* (6), 1644-1650.
(23) Sharma, A.; Mahlouji, R.; Wu, L.; Verheijen, M. A.; Vandalon, V.; Balasubramanyam, S.; Hofmann, J. P.; Erwin Kessels, W. M. M.; Bol, A. A. Large area, patterned growth of 2D $MoS_2$ and lateral $MoS_2$-$WS_2$ heterostructures for nano- and opto-electronic applications. *Nanotechnology* **2020**, *31* (25), 255603.
(24) Mahlouji, R.; Verheijen, M. A.; Zhang, Y.; Hofmann, J. P.; Kessels, W. M. M.; Bol, A. A. Thickness and Morphology Dependent Electrical Properties of ALD-Synthesized $MoS_2$ FETs. *Advanced Electronic Materials* **2021**, *8* (3), 2100781.
(25) Zabrosaev, I. V.; Kozodaev, M. G.; Romanov, R. I.; Chernikova, A. G.; Mishra, P.; Doroshina, N. V.; Arsenin, A. V.; Volkov, V. S.; Koroleva, A. A.; Markeev, A. M. Field-Effect Transistor Based on 2D Microcrystalline $MoS_2$ Film Grown by Sulfurization of Atomically Layer Deposited $MoO_3$. *Nanomaterials* **2022**, *12* (19), 3262.
(26) Aspiotis, N.; Morgan, K.; März, B.; Müller-Caspary, K.; Ebert, M.; Weatherby, E.; Light, M. E.; Huang, C. C.; Hewak, D. W.; Majumdar, S.; et al. Large-area synthesis of high electrical performance $MoS_2$ by a commercially scalable atomic layer deposition process. *npj 2D Mater. Appl.* **2023**, *7* (1), 18.
(27) Choudhary, N.; Park, J.; Hwang, J. Y.; Choi, W. Growth of large-scale and thickness-modulated $MoS_2$ nanosheets. *ACS Appl. Mater. Interfaces* **2014**, *6* (23), 21215-21222.
(28) Ohashi, T.; Suda, K.; Ishihara, S.; Sawamoto, N.; Yamaguchi, S.; Matsuura, K.; Kakushima, K.; Sugii, N.; Nishiyama, A.; Kataoka, Y.; et al. Multi-layered $MoS_2$ film formed by high-temperature sputtering for enhancement-mode nMOSFETs. *Jpn. J. Appl. Phys.* **2015**, *54* (4), 04DN08.
(29) Tao, J.; Chai, J.; Lu, X.; Wong, L. M.; Wong, T. I.; Pan, J.; Xiong, Q.; Chi, D.; Wang, S. Growth of wafer-scale $MoS_2$ monolayer by magnetron sputtering. *Nanoscale* **2015**, *7* (6), 2497-2503.
(30) Huang, J. H.; Chen, H. H.; Liu, P. S.; Lu, L. S.; Wu, C. T.; Chou, C. T.; Lee, Y. J.; Li, L. J.; Chang, W. H.; Hou, T. H. Large-area few-layer $MoS_2$ deposited by sputtering. *Mater. Res. Express* **2016**, *3* (6), 065007.
(31) Hussain, S.; Singh, J.; Vikraman, D.; Singh, A. K.; Iqbal, M. Z.; Khan, M. F.; Kumar, P.; Choi, D. C.; Song, W.; An, K. S.; et al. Large-area, continuous and high electrical performances of bilayer to few layers $MoS_2$ fabricated by RF sputtering via post-deposition annealing method. *Sci Rep* **2016**, *6*, 30791.
(32) Ishihara, S.; Hibino, Y.; Sawamoto, N.; Suda, K.; Ohashi, T.; Matsuura, K.; Machida, H.; Ishikawa, M.; Sudoh, H.; Wakabayashi, H.; et al. Improving crystalline quality of sputtering-deposited $MoS_2$ thin film by postdeposition sulfurization annealing using $(t\text{-}C_4H_9)_2S_2$. *Jpn. J. Appl. Phys.* **2016**, *55* (4), 04EJ07.
(33) Samassekou, H.; Alkabsh, A.; Wasala, M.; Eaton, M.; Walber, A.; Walker, A.; Pitkänen, O.; Kordas, K.; Talapatra, S.; Jayasekera, T.; et al. Viable route towards large-area 2D $MoS_2$ using magnetron sputtering. *2D Mater.* **2017**, *4* (2), 021002.

(34) Samassekou, H.; Alkabsh, A.; Stiwinter, K.; Khatri, A.; Mazumdar, D. Atomic-level insights through spectroscopic and transport measurements into the large-area synthesis of $MoS_2$ thin films. *Mrs Communications* **2018**, *8* (3), 1328-1334.
(35) Hasuike, N.; Yamauchi, S.; Seki, K.; Kamoi, S.; Nishio, K.; Kisoda, K. Optical characterization of $MoS_2$ sputtered thin films. *J Phys Conf Ser* **2019**, *1220*, 012057.
(36) Qi, M.; Xiao, J. R.; Gong, C. Y. Thermal annealing effects on the electrophysical characteristics of sputtered $MoS_2$ thin films by Hall effect measurements. *Semicond. Sci. Technol.* **2019**, *34* (4), 045017.
(37) Park, H.; Liu, N.; Kim, B. H.; Kwon, S. H.; Baek, S.; Kim, S.; Lee, H. K.; Yoon, Y. J.; Kim, S. Exceptionally Uniform and Scalable Multilayer $MoS_2$ Phototransistor Array Based on Large-Scale $MoS_2$ Grown by RF Sputtering, Electron Beam Irradiation, and Sulfurization. *ACS Appl. Mater. Interfaces* **2020**, *12* (18), 20645-20652.
(38) Acar, M. One step sputtered $MoS_2$ field-effect transistor. *Micro and Nanostructures* **2022**, *165*, 207203.
(39) Subramaniyam, S.; Bharatan, S.; Muthusamy, S.; Sivaprakasam, S. Effects of Substrate Biasing and Sulfur Annealing on the Surface of $MoS_2$ Thin Films and TFT. *Coatings* **2025**, *15* (2), 146.